Migration of breast cancer cells: Understanding the roles of volume exclusion and cell-to-cell adhesion

Matthew J. Simpson,[1,2] Chris Towne,[2] D. L. Sean McElwain,[1,2] and Zee Upton[2]
[1]*Mathematical Sciences, Queensland University of Technology, Brisbane, Australia*
[2]*Tissue Repair and Regeneration Program, Institute of Health and Biomedical Innovation (IHBI), Queensland University of Technology, Brisbane, Australia*
(Received 9 June 2010; revised manuscript received 29 July 2010; published 1 October 2010)

We study MCF-7 breast cancer cell movement in a transwell apparatus. Various experimental conditions lead to a variety of monotone and nonmonotone responses which are difficult to interpret. We anticipate that the experimental results could be caused by cell-to-cell adhesion or volume exclusion. Without any modeling, it is impossible to understand the relative roles played by these two mechanisms. A lattice-based exclusion process random-walk model incorporating agent-to-agent adhesion is applied to the experimental system. Our combined experimental and modeling approach shows that a low value of cell-to-cell adhesion strength provides the best explanation of the experimental data suggesting that volume exclusion plays a more important role than cell-to-cell adhesion. This combined experimental and modeling study gives insight into the cell-level details and design of transwell assays.

DOI: 10.1103/PhysRevE.82.041901 PACS number(s): 87.17.Aa, 87.10.Rt, 87.17.Jj

I. INTRODUCTION

Cell-to-cell contact and cell crowding effects are known to regulate cell migration. These effects, often called contact inhibition of migration [1], can be particularly important when cells are in close contact and volume exclusion can limit opportunities for cell migration [2–4]. Traditional continuum models of cell motility based on linear advection diffusion models [5–7] or noninteracting discrete random-walk models [8] ignore these effects. To overcome this difficulty, a class of lattice-based random-walk models called exclusion processes [9] have been used to model cell motility. These models introduce a simple and biologically realistic mechanism to enforce volume exclusion by permitting each lattice site to be occupied by, at most, one agent [10–17].

Cell-to-cell adhesion is also thought to play a role regulating cell motility in many cell biology systems [18–20]. Although the importance of cell-to-cell adhesion is widely acknowledged, many mathematical models of cell motility simply ignore cell-to-cell adhesion [5–8]. Results from those models that do incorporate some cell-to-cell adhesion mechanism are often compared with biological data qualitatively rather than quantitatively [12,15,21,22]. In contrast, recent work by Deroulers *et al.* [23] reported the development of a discrete cell motility model using experimentally motivated agent-to-agent adhesion mechanisms. The model presented by Deroulers *et al.* [23] was able to quantitatively replicate experiments describing the movement of cells from a glioma spheroid.

In this work we describe experimental results for a transwell migration assay where we anticipate that cell-to-cell adhesion and volume exclusion effects could be relevant. To explore the relative importance of volume exclusion and cell-to-cell adhesion, we apply a mathematical model to replicate the transwell experiments. To model this system we take a similar approach to Deroulers *et al.* [23] and apply a model that incorporates both volume exclusion effects and agent-to-agent adhesion. This combined experimental and modeling study gives insight into the cell-level detail and design of transwell assays.

II. TRANSWELL CELL MIGRATION ASSAY

Three types of experiments characterizing the migration of MCF-7 breast cancer cells [24] through a transwell apparatus [25] were performed. A schematic of the transwell apparatus is given in Fig. 1(a). In each experiment, a known number of MCF-7 cells were placed in the upper compartment (N_U), and the number of cells that migrated through the porous membrane into the lower compartment (N_L) was determined at particular times. Full details of the experimental procedure have been described elsewhere [26,27]. Briefly, the MCF-7 cell line (ATCC No. HTB-22) was obtained from Myers (Centre for Molecular Biotechnology, Queensland University of Technology) and grown in Dulbecco's Modified Eagle's/Ham's F12 (DMEM-F12) media (1:1) (Life Technologies, Mulgrave, Victoria, Australia) containing 10% fetal calf serum, 50 units/ml penicillin G, 50 μm/ml streptomycin sulfate, and 0.1 μl gentamicin. Media were changed every second day and cells passaged when confluent using 0.25% trypsin/0.5 mM ethylenediamine tetra-acetic acid (EDTA) solution (Oxoid, Hampshire, England). All assays were performed using cells from passages 24 to 34.

1 μg of human Vitronectin (VN) (Promega, Armadale, New South Wales, Australia) in serum-free SMEM-F12 was added to the lower compartment of the transwell apparatus and incubated at 37 °C for 2 h. Media containing unbound VN were then removed and the lower compartments washed twice with Hepes binding buffer containing 0.5% bovine serum albumin (BSA) (RIA grade fraction V, Sigma Aldrich, Castle Hill, New South Wales, Australia). Purified human recombinant IGF (GroPrep, Adelaide, South Australia, Australia) was resuspended in 10 mM HCl as per the manufacturer's instructions, diluted in 0.05% BSA/DMEM-F12 and added to the lower compartment of the transwells. This so-

 ©2010 The American Physical Society

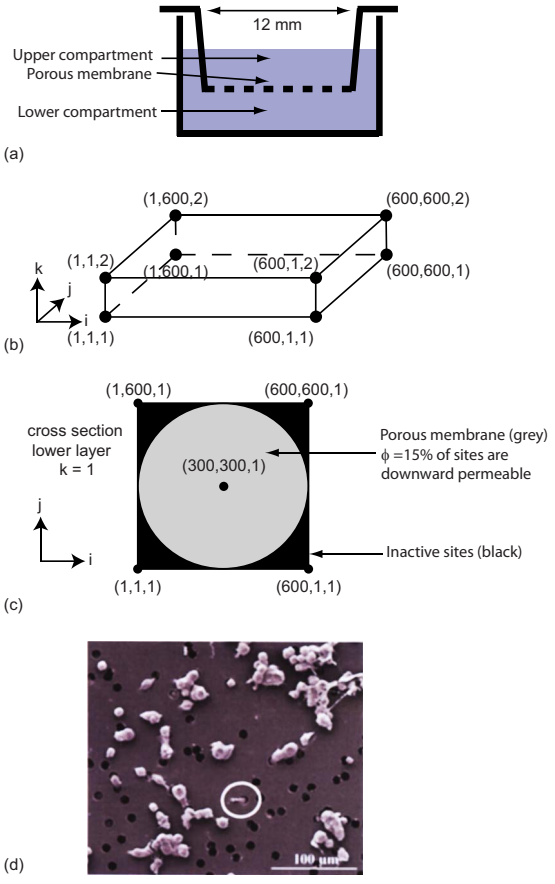

FIG. 1. (Color online) (a) Schematic of the transwell apparatus, adapted from [25]. (b) A 3D cuboid region defines the geometry of the random-walk model in terms of the (i,j,k) lattice indices. This 3D cuboid region is used to embed the cylindrical transwell geometry. (c) A cross section through the cuboid region where $k=1$ shows the location of the porous membrane shaded gray (light gray) and the inactive sites are shaded black (black). (d) Image from a scanning electron microscope shows several MCF-7 breast cancer cells sitting on the upper surface of a transwell membrane. The cells are white (white) and are clearly distinct from the black pores (black). This image highlights a particular cell (circled) moving through a pore (image is reproduced with kind permission from Kricker [30]).

lution contained 10–100 ng of $[L^{27}]$ IGF-II. These growth factors were then allowed to bind to the VN-coated lower compartments for 2 h at 37 °C or overnight at 4 °C. The media containing unbound growth factors were removed and the lower compartment washed twice with 0.05% BSA/DMEM-F12. The transwells were air dried in laminar flow hoods with 0.05% BSA/DMEM-F12 added to the lower compartment immediately before commencement of the assays. We use this procedure to study cell migration in the presence of VN and various concentrations of IGF-II ranging from 0 to 100 ng/ml. Although these concentrations of IGF-II are less than the concentrations observed in human serum [28,29], previous transwell experiments have shown that these levels of VN and IGF-II are sufficient to enhance the migration of MCF-7 cells [27].

70% confluent growth phase cultures of MCF-7 cells were passaged at a ratio of 1:1 the day prior to the assay. The next morning cells were serum starved for 4 h and harvested with 0.25% trypsin/0.5 mM EDTA solution. Trypsinized cells were resuspended in serum-free media and centrifuged at 400 g for 10 min. The Trypsin-free cell pellet was then resuspended in 0.05% BSA/DMEM-F12 and the cells were counted using a hemocytometer. Cells were diluted to a density of 1×10^6 cells/ml and then the appropriate number of cells, N_U, was placed in the upper compartment of the transwell. After the assay, the transwell inserts were incubated at 37 °C in 5% CO_2 for 5 h. Cells that had migrated through the porous membrane were fixed in 37% formaldehyde and stained with 0.01% crystal violet in 0.1 mM borate buffer (pH 9). The number of cells that migrated through the porous membrane was quantified by extracting the crystal violet stain in 10% acetic acid and determining the optical density of these extracts at 595 nm. All experiments were repeated three times ($n=3$) and mean results are presented, with error bars defined by the standard error.

Our combined experimental and modeling study is motivated by the need to improve standard transwell assay design. Traditionally, transwell assays have been designed and analyzed heuristically by comparing the number of cells that move through a transwell, during a fixed period of time, relative to some control condition [26,27,30–32]. This kind of heuristically designed assay provides little understanding about the influence of varying the timing of the experiment or placing different numbers of cells in the transwell. Our combined experimental and mathematical approach aims to overcome these previous limitations by providing quantitative insight into the cell-level details of transwell assays. Three sets of experiments were performed as follows:

In the *time course experiments*, VN and IGF-II (5 ng/ml) were placed in the lower compartment of the transwell. Experiments were initiated by seeding $N_U=200\,000$ MCF-7 cells into the upper compartment of the transwell and N_L was determined at particular points in time $T\in[1,9]$ h. Results in Fig. 2(a) show that N_L increased monotonically, and approximately linearly, with time.

The time course experiments were conducted for no longer than 9 h and the remaining experiments (described subsequently) were conducted for no longer than 5 h. To interpret the transwell assays we neglect any increase in cell number due to cell division. There are two aspects of the experimental system that allow us to neglect cell division. First, estimates of the doubling time of MCF-7 cells range from 24 to 38 h [33,34]. This means that the timing of the transwell assays is much shorter than the cell cycle time scale, so that most cells will not have enough time to divide during the assay. Second, the MCF-7 cells were in a serum-free medium.

For the *cell seeding experiments*, VN and IGF-II (5 ng/ml) were placed in the lower compartment of the transwell. Various numbers of MCF-7 cells, $N_U\in[10\,000,400\,000]$, were seeded into the upper compartment and N_L was determined after 5 h. Results in Fig. 2(b) show that N_L increased with N_U, provided that $N_U<300\,000$. A reduction in migration was observed when $N_U>300\,000$. This threshold behavior implies that some mechanism, activated at high cell densities, reduces the cell migration ability. One of the objectives of this work is to investigate the origin of this threshold behavior.

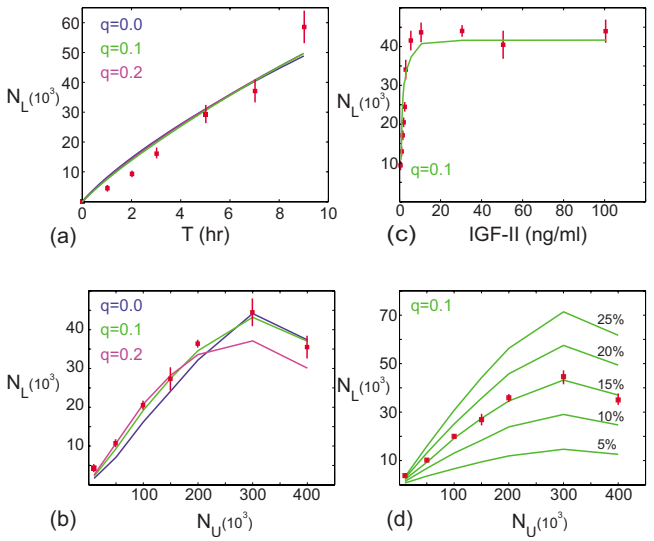

FIG. 2. (Color online) Experimental results are shown as red squares and modeling results are shown as green, purple, and blue solid lines (light gray, medium gray, and dark gray). These results correspond to (a) the time course experiments where N_L was measured at various times after placing $N_U=200\,000$ cells into the upper compartment with 5 ng/ml IGF-II in the lower chamber, (b) the cell seeding experiments show N_L after 5 h for various $10\,000 \le N_U \le 400\,000$ with 5 ng/ml IGF-II in the lower chamber, and (c) the growth factor experiments show N_L after 5 h for $N_U=200\,000$ and various concentrations of IGF-II. Modeling results in (a)–(c) correspond to (i) $\Delta=20$ μm, $P=0.1$, $q=0.0$, and $\tau=0.11$ h shown in blue (dark gray); (ii) $\Delta=20$ μm, $P=0.1$, $q=0.1$, and $\tau=0.08$ h shown in green (light gray); and (iii) $\Delta=20$ μm, $P=0.1$, $q=0.2$, and $\tau=0.06$ h shown in purple (medium gray). We note that each modeling profile in (a) has been rescaled to fit the experimental data, so that it is difficult to distinguish between the three modeling curves. Modeling results in (c) correspond to $\Delta=20$ μm, $q=0.1$, $\tau=0.08$ h, and $P(C)=0.025+(0.1C)/(1+C)$. Results in (d) are the same as (b) with different proportions of pore space, 5%, 10%, 15%, 20%, and 25%, as indicated. All simulation results are averaged over $n=20$ identically prepared realizations. The discrete model was used to predict the migration assays with the same data points as the experiments and linear interpolation was used to generate the profiles in (a)–(d).

In the *growth factor experiments*, VN and various concentrations of IGF-II $\in[0,100]$ ng/ml were placed in the lower compartment of the transwell. For each concentration of IGF-II, $N_U=200\,000$ MCF-7 cells were seeded into the upper compartment and N_L was measured after 5 h. Figure 2(c) shows that the migration of MCF-7 cells was stimulated by the presence of IGF-II. Furthermore, a saturation effect was observed where the increase in migration occurred for small concentrations of IGF-II only, and no further stimulation of migration occurred once the concentration of IGF-II is sufficiently large.

III. DISCRETE RANDOM-WALK MODEL

To interpret the experimental observations we need to understand the relevant cell-level mechanisms that govern the movement of cells through the transwell. One way to do this is to apply a mathematical model [35] to the system and replicate the observed experimental data [36,37]. We hypothesize that the observed nonmonotone behavior in the cell seeding experiments could be caused either by (1) cell-to-cell adhesion, where cell-to-cell attachments are more likely to form and prevent cells moving through the porous membrane when $N_U > 300\,000$, or (2) volume exclusion and crowding effects near the porous membrane, whereby local crowding restricts the movement of cells through the pores in the porous membrane when $N_U > 300\,000$. The goal of the modeling exercise is to understand the relative roles of these two mechanisms and gain deeper insight into the relevant cell-level mechanisms that drive cell migration in a transwell.

We apply a discrete random-walk model to replicate the experimental data. The discrete model is an extension of the models described by Khain and co-workers [11–13]. This model is related to a three-dimensional (3D) asymmetric exclusion process on a square lattice with spacing Δ [9]. Each lattice site is indexed (i,j,k), where $i,j,k \in \mathbb{Z}^+$, and each site has position $(x,y,z)=(\Delta i, \Delta j, \Delta k)$. Cells are idealized as incompressible agents and computational realizations are made using a random sequential update algorithm [38] described as follows: if there are N agents on the lattice, during the next time step of duration τ, N agents are selected independently at random, one at a time. When chosen, an agent attempts to move with probability $P(1-q)^a$. Here, $P \in [0,1]$ is the probability that an isolated agent can move a distance Δ during the time interval τ, $q \in [0,1)$ is a measure of agent adhesiveness, and $a \in [0,6]$ is the number of occupied nearest-neighbor lattice sites of that agent [12,13]. With regard to the direction of motion, a motile agent at site (i,j,k) attempts to step to (i) $(i \pm 1,j,k)$ with probability $(1 \pm \rho_x)/6$, (ii) $(i,j \pm 1,k)$ with probability $(1 \pm \rho_y)/6$, or (iii) $(i,j,k \pm 1)$ with probability $(1 \pm \rho_z)/6$. The parameters $\rho_x \in [-1,1]$, $\rho_y \in [-1,1]$, and $\rho_z \in [-1,1]$ control the motility bias; setting $\rho_x=\rho_y=\rho_z=0$ means that the motion is unbiased. If an agent attempts to step to an occupied site, then that motility event is aborted.

With $q=0$, the model becomes an asymmetric simple exclusion process [14]. With $q>0$, the model is more complicated because adhesion between agents makes it harder for an agent to move. This mechanism is a simple way to incorporate the effect of adhesion between agents, and the value of q provides a measure of the adhesive strength [12,13]. In the Appendix we present and analyze several sets of simulation data to demonstrate the effect of varying q.

IV. APPLYING THE DISCRETE MODEL TO THE TRANSWELL EXPERIMENTS

The transwell is cylindrical with an inner diameter of 12 mm [25] and MCF-7 breast cancer cells are approximately 20 μm in diameter [30]. We represent the upper compartment of the transwell using a 3D lattice with spacing $\Delta=20$ μm, so that the lattice spacing is equal to the average cell diameter [12,13]. The 3D lattice has two layers in the vertical direction giving $1 \le k \le 2$. Each layer of the lattice is a square with length $1 \le i \le 600$ and width $1 \le j \le 600$. The length and width are chosen to accommodate the 20 μm

MCF-7 cells in the 12 mm transwell, giving $12/(0.02)=600$. To represent the cylindrical geometry, all sites in the region $(i-300)^2+(j-300)^2 \leq 300^2$ can be occupied by agents, and we call these *active* sites. The remaining sites where $(i-300)^2+(j-300)^2 > 300^2$ are *inactive* and cannot be occupied. Any potential motility event that would place an agent on an inactive site is aborted. This configuration embeds the cylindrical geometry of the transwell into a simple cuboid region shown in Fig. 1(b). Each layer in the lattice contains approximately $\pi 300^2 \approx 282\,743$ active sites.

The porous membrane separates the upper and lower compartments [Fig. 1(a)] and the membrane is approximately 15% pore space [25]. Scanning electron micrographs [Fig. 1(d)] show several MCF-7 cells on the porous membrane of a transwell [30]. Although MCF-7 cells are larger than the pore diameter (approximately 12 μm [25]), we observe that the cells are able to move through the pore space [Fig. 1(d)]. We take a simple but realistic approach to modeling the movement of cells through the membrane pores. In any single realization of the model we represent the porous membrane by randomly selecting 15% of the active sites on the lower $(k=1)$ layer of the lattice and assume that these sites represent a pore in the membrane. We call these sites *downward permeable sites*. The remaining 85% of active sites on the lower $(k=1)$ layer are *downward impermeable sites*, and these sites represent the solid impermeable part of the membrane. This means that a motile agent residing on a downward impermeable site (i,j,k) steps to (i) $(i\pm 1,j,k)$ with probability $(1\pm\rho_x)/6$, (ii) $(i,j\pm 1,k)$ with probability $(1\pm\rho_y)/6$, and (iii) $(i,j,k+1)$ with probability $(1+\rho_z)/6$ and $(i,j,k-1)$ with probability zero owing to the presence of the porous membrane. In comparison, a motile agent residing on a downward permeable site (i,j,k) is permitted to move in the negative z direction in the usual way as this agent is not blocked by the membrane.

During the transwell assays, cells are placed in the upper compartment and rapidly settle onto the porous membrane. To represent this, we place agents on the lattice to mimic the way that cells are distributed after they have settled onto the porous membrane. For example, to model an experiment with $N_U=200\,000$ cells, we initially randomly occupy $70.7\%=100\times 200\,000/282\,743$ of active lattice sites on the lower $(k=1)$ layer of the lattice. Similarly, to model an experiment with $N_U=400\,000$ cells, we initially occupy $100\%=100\times 282\,743/282\,743$ of active lattice sites on the lower $(k=1)$ layer and then randomly occupy $41.5\%=100\times 117\,257/282\,743$ of active sites on the upper $(k=2)$ layer of the lattice. Since we are modeling experiments with no more than $N_U=400\,000$, we only require two vertical layers in the 3D lattice to accommodate this number of cells. To represent the movement of cells in the transwell experiments we set $\rho_z=-1$. This prevents agents moving vertically upward, which is consistent with our observations of cell movement in a transwell. We also set $\rho_x=\rho_y=0$, which is appropriate because there is no observed bias in the movement of cells in the horizontal plane.

During the simulations some agents move vertically down through the pore space in the lower layer of the lattice. We assume that these agents leave the system and no longer interact with other agents during that simulation. Other potential movement events that would place an agent outside the cuboid region [Fig. 1(b)] are aborted. To match the model predictions and experimental data, we count the number of agents leaving the system through the lower layer of the lattice, giving N_L. Owing to the stochastic nature of the algorithm, $n=20$ identically prepared realizations of each simulation were performed, and average results are presented [14,15].

V. CHOOSING THE MODEL PARAMETERS

We now explain how the parameters in the discrete model were chosen. Experimental data for the time course experiments [Fig. 2(a)] show an approximately linear increase in N_L from $N_L=0$ at $T=0$ to $N_L=59\,000$ at $T=9$. To match this data we performed several simulations of each time course experiment. In each simulation we used a different value of the adhesion parameter $(q=0.0,0.1,0.2,0.3,0.4,0.5,0.6)$ together with a nondimensional time step $\bar{\tau}=1$. To fit the data to the experimental observations, we rescaled the nondimensional time step to give a real dimensional time step τ. The value of τ was chosen to minimize the discrepancy between the modeling and experimental data, measured by

$$E=\sum_{i=1}^{M}|N_L^{\text{experiment}}-N_L^{\text{model}}|, \tag{1}$$

where $N_L^{\text{experiment}}$ is the experimental data, N_L^{model} is the predicted data, and M is the number of data points used to fit the data sets. Using this procedure, we identified a different optimal value of τ for each value of the adhesion parameter q. For example, with $q=0.0$, $\tau=0.11$ gave the best fit to the data, while for $q=0.1$, we found that $\tau=0.08$ gave the best fit to the data. With the rescaled data, we can now plot a family of curves for the time course experiments showing how N_L varies with time for each value of q. A subset of these curves, for $q=0,0.1,0.2$, is given in Fig. 2(a) showing that each simulated curve matches the experimental data, and it is impossible to distinguish which of these curves best matches the time course data. The high quality of fit between the simulated and the experimental data in Fig. 2(a) is expected because we have chosen to rescale the simulation time to give the best fit to the data. For simplicity, only three results for $q=0.0,0.1,0.2$ are shown in Fig. 2(a). We will show subsequently that these three profiles are the most relevant.

Now that we have used the time course experimental data to arrive at an optimal value of τ for each value of q, we then tested whether these sets of parameters could independently predict the cell seeding experiments. This procedure gave several sets of simulation data describing N_L at $T=5$ for each value of N_U. Three of these sets of simulation data, for $q=0.0,0.1,0.2$, are superimposed on the experimental data in Fig. 2(b). From these results we see that the profiles for $q=0.0$ and $q=0.1$ replicate the experimental data reasonably well. In comparison, the profile for $q=0.2$ fails to match the experimental data. Similarly, all simulations with $q>0.1$ failed to match the experimental data for the cell seeding experiments. In summary, this procedure showed that setting $q>0.1$ could not predict both the time course assay and the

cell seeding experiments simultaneously. Using Eq. (1) to measure the goodness of fit between the experimental data and the simulation data we conclude that the simulation results in Fig. 2(b) with $q=0.1$ give the best match to the experimental data.

Given that a small value of q provides the best fit to the experimental data, our modeling suggests that volume exclusion appears to play a more important role than cell-to-cell adhesion. In particular, we note that simulations of the cell seeding experiments with no agent-to-agent adhesion ($q=0.0$) also predicts a nonmonotone profile for the cell seeding experiments that is a reasonable approximation to the experimental data. These results suggest that the nonmonotone experimental profile is driven by volume exclusion where agent crowding around the membrane pores reduces the ability of the total population to move into the lower chamber of the transwell for sufficiently large N_U. Similar effects are observed in models of human evacuation which involve volume exclusion and directed motion toward relatively small exit spaces [39]. We also remark that the importance of crowding effects is consistent with the observation that the maximum value of N_L in Fig. 2(b) occurs when $N_U=300\,000$. Given that $\pi 300^2 \approx 282\,743$ MCF-7 cells can be evenly distributed in a confluent monolayer across the porous membrane, we expect that crowding effects are likely to become significant and change the response of the system around $N_U=\pi 300^2$.

Given that the best fit to the experimental data was for $P=0.1$, $q=0.1$, and $\tau=0.08$ h, we can deduce that the characteristic time required for a cell to move a distance equal to the cell diameter (20 μm) is 48 min. This measure of the characteristic time of motility is comparable to other estimates that have been derived by applying exclusion process-based models to experimental data. For example, Deroulers and co-workers [23] found that their experimental observations were best explained using a cell diffusivity that corresponded to a characteristic time of motility of 15 min. Given that literature values of cell diffusivities vary over two orders of magnitude [40], our estimate of the time scale of motility is consistent with known values from the literature.

We would like to emphasize that these modeling results illustrate the importance of using an appropriate model to represent the transwell experiments. As we have previously mentioned, standard continuum models of cell motility, based on linear advection-diffusion mechanisms [5,6,41] or standard random-walk models that ignore volume exclusion [8], cannot predict the kind of nonmonotone behavior observed in the cell seeding experiments. A model that ignores volume exclusion effects would predict a monotone response for the cell seeding experiment, which is clearly inappropriate for this system.

To model the growth factor experiments we follow previous approaches and relate the unbiased component of the cell motility to concentration of IGF-II [42,43]. Assuming that the total number of growth factor receptor sites on each cell (R_0) is composed of the sum of free (R_f) and bound (R_b) sites we require

$$R_0 = R_f + R_b. \tag{2}$$

Equating the time rate of change of the number of bound receptor sites to the difference between the rates of association and dissociation gives

$$\frac{dR_b}{dt} = k_1 C R_f - k_2 R_b, \tag{3}$$

where k_1 is an association rate coefficient, k_2 is a dissociation rate coefficient, and C is the growth factor concentration. Assuming the association-dissociation dynamics have reached equilibrium and $dR_b/dt=0$, we combine Eqs. (2) and (3) to obtain a relationship between the number of bound sites and the growth factor concentration,

$$R_b = R_0 \frac{k_1 C}{(k_1 C + k_2)}. \tag{4}$$

Assuming the net motility can be expressed as the sum of the intrinsic motility and an additional component that is proportional to R_b, we obtain

$$P(C) = P_0 + \lambda R_b = P_0 + R_0 \frac{\lambda k_1 C}{(k_1 C + k_2)}. \tag{5}$$

This relationship between probability of motility and the growth factor concentration has the form of a Monod relationship which has been used by others to represent chemokinetic effects [44]. The general form of the Monod model is given by

$$P(C) = P_0 + \frac{AC}{B + C}, \tag{6}$$

where C is the concentration of IGF-II (ng/ml), P_0 is the motility of cells in the absence of growth factor where $C=0$ ng/ml, A represents the growth factor-enhanced probability of motility, and B is the half-saturation concentration.

By using the Monod relationship [Eq. (6)] we assume that IGF-II enhances cell migration through stimulating the undirected component of cell motility (chemokinesis) rather than stimulating directed cell motility (chemotaxis) [45]. This is appropriate for the transwell assay because we have already modeled a bias in migration in the negative z direction in order to prevent agents moving upward during the simulations. This bias effect, caused by gravity, is independent of the motility stimulation caused by the presence of growth factors. It is therefore most appropriate to relate the enhanced migration caused by IGF-II to the unbiased component of motility. Results in Fig. 2(c) with $P_0=0.025$, $A=0.1$, and $B=1$ show that the Monod model is able to describe the effects of IGF-II on this system and captures both the stimulation of motility effect for low concentrations of IGF-II and the saturation effect observed at higher values of IGF-II.

By matching experimental data with the results from a mathematical model, we have demonstrated that crowding effects caused by volume exclusion are likely to give rise to the nonmonotone results for the cell seeding experiments. To further examine this result, we present additional simulations predicting the influence of varying the porosity of the membrane. Results in Fig. 2(d) use the same parameters for the

time course and cell seeding experiments ($q=0.1$, $P=0.1$, $\tau=0.08$ h) and predict how the porosity of the membrane affects the transwell experiments. In our previous simulations [Figs. 2(a)–2(c)], we represented the porosity of the membrane by randomly selecting 15% of lattice sites on the lower layer ($k=1$) and making those sites downward permeable sites. To extend these details we repeat our simulations of the cell seeding experiments but now vary the number of downward permeable sites (5%, 10%, 15%, 20%, and 25%) and compare the model predictions for these different membrane porosities in Fig. 2(d). As expected, more agents pass through the membrane as the number of downward permeable sites increases. Furthermore, we see that the nonmonotone profiles are ubiquitous and the turning point in the N_L profiles always occur near $N_U=300\,000$ for reasons previously explained.

VI. DISCUSSION AND CONCLUSION

By using an appropriate mathematical model incorporating effects of volume exclusion and cell-to-cell adhesion, we have been able to choose the parameters in the model to give a best fit to a detailed set of transwell migration assays. This procedure showed that it was only possible to match the experimental data using a small value of the adhesion parameter $q=0.1$. This suggests that the effects of volume exclusion are more important than the effects of cell-to-cell adhesion for these sets of experiments. We emphasize that this result was not obvious prior to matching the experimental and modeling results. We also make the point that this modeling study emphasizes the importance of using an appropriate model to represent the system of interest. As we have pointed out, standard mathematical models of cell motility are inappropriate for this kind of assay because they simply ignore volume exclusion and cell-to-cell adhesion.

This modeling study provides us with a quantitative tool that can be used to both design and interpret transwell assays. Previously, transwell assays were designed and analyzed heuristically by comparing cell migration through a transwell relative to some control conditions [26,27,30–32]. Experimental results describing the migration ability of cells in this type of heuristically designed assay were always measured in terms of "percent of negative control" [26,27,30–32]. Although this kind of measurement is able to identify whether growth factors placed in the lower chamber of the transwell could stimulate migration, the traditional approach gave no insight into the effect of altering the assay design. For example, these previous approaches gave no insight into the effect of altering N_U or altering the timing of the migration assay. Instead, our current work offers a biologically motivated mathematical approach to understand transwell assays leading to deeper insight into relevant biological mechanisms.

ACKNOWLEDGMENTS

We thank Ruth Baker and Prabhakar Clement for their comments on a draft form of this manuscript. We also thank Jennifer Kricker for kind permission to reproduce an image from her Ph.D. thesis and Abhishek Kashyap for his kind assistance. Z.U. and D.L.S.M. acknowledge the support from the QUT ATN Scheme and the Queensland Cancer Fund.

APPENDIX: SIMULATION DATA AND ANALYSIS OF THE AGENT-TO-AGENT ADHESION MODEL

In this appendix we give a physical and mathematical interpretation of the random-walk model used to represent the transwell experiments. Previous investigations have analyzed this model in terms of the relationship between the unbiased adhesive random-walk model and the Ising model [13]. Here, we demonstrate how the random-walk model relates to a partial differential equation (pde) model in the appropriate limit. Our analysis is relevant for both unbiased ($\rho_x=\rho_y=0$) and biased ($\rho_x\neq 0$, $\rho_y\neq 0$) motilities.

To gain insight into the physics of the problem, we consider the same random-walk model used in the main text on a simpler two-dimensional (2D) square lattice with spacing Δ. Each lattice site is indexed (i,j), where $i,j\in\mathbb{Z}^+$, and each site has position $(x,y)=(\Delta i,\Delta j)$. To connect the discrete mechanism with its continuum counterpart, we average the occupancy of site (i,j) over many statistically identical realizations to obtain $\langle C_{i,j}\rangle\in[0,1]$ [14–16]. After averaging, we form a discrete conservation statement describing $\delta\langle C_{i,j}\rangle$, which is the change in average occupancy of site (i,j) during the time interval from t to $t+\tau$. The discrete conservation statement is given by

$$\begin{aligned}\delta\langle C_{i,j}\rangle = {}& \frac{P(1+\rho_x)}{4}\langle C_{i-1,j}\rangle(1-\langle C_{i,j}\rangle)(1-q)^{\Sigma C_{i-1,j}} \\ & + \frac{P(1-\rho_x)}{4}\langle C_{i+1,j}\rangle(1-\langle C_{i,j}\rangle)(1-q)^{\Sigma C_{i+1,j}} \\ & + \frac{P(1+\rho_y)}{4}\langle C_{i,j-1}\rangle(1-\langle C_{i,j}\rangle)(1-q)^{\Sigma C_{i,j-1}} \\ & + \frac{P(1-\rho_y)}{4}\langle C_{i,j+1}\rangle(1-\langle C_{i,j}\rangle)(1-q)^{\Sigma C_{i,j+1}} \\ & - \frac{P(1+\rho_x)}{4}\langle C_{i,j}\rangle(1-\langle C_{i+1,j}\rangle)(1-q)^{\Sigma C_{i,j}} \\ & - \frac{P(1-\rho_x)}{4}\langle C_{i,j}\rangle(1-\langle C_{i-1,j}\rangle)(1-q)^{\Sigma C_{i,j}} \\ & - \frac{P(1+\rho_y)}{4}\langle C_{i,j}\rangle(1-\langle C_{i,j+1}\rangle)(1-q)^{\Sigma C_{i,j}} \\ & - \frac{P(1-\rho_y)}{4}\langle C_{i,j}\rangle(1-\langle C_{i,j-1}\rangle)(1-q)^{\Sigma C_{i,j}}, \quad \text{(A1)}\end{aligned}$$

where

$$\sum C_{\alpha,\beta}=\langle C_{\alpha,\beta+1}\rangle+\langle C_{\alpha,\beta-1}\rangle+\langle C_{\alpha-1,\beta}\rangle+\langle C_{\alpha+1,\beta}\rangle. \quad \text{(A2)}$$

The four positive terms on the right of Eq. (A1) represent motility events that increase the average occupancy of site (i,j), and the four negative terms on the right of Eq. (A1)

represent motility events that decrease the average occupancy of site (i,j). To derive this discrete conservation statement we have made the standard assumption that the occupancy status of lattice sites is independent. This assumption, while questionable for any single realization of the discrete model, is known to be an excellent approximation in other exclusion process-based discrete models [14,15,23]. Our discrete-continuum comparisons, shown below, confirms that these assumptions are reasonable provided that q is sufficiently small, $q \leq 0.5$. Further simulation data (not shown here) confirm that the continuum model fails to predict the discrete simulation data when q is sufficiently large, $q > 0.5$. Therefore, the assumptions made to arrive at the continuum model appear to be less reliable as q increases. This difficulty is irrelevant to the transwell data since we have shown that the experiments correspond to a small value of $q=0.1$.

The discrete conservation statements are related to a pde model in the appropriate limit as $\Delta \to 0$ and $\tau \to 0$, and $\langle C_{i,j} \rangle$ is written in terms of a continuous variable $C(x,y,t)$. To see this relationship, all terms in Eqs. (A1) and (A2) are expanded in a Taylor series about site (i,j), keeping terms up to $\mathcal{O}(\Delta^2)$. Dividing the resulting expression by τ, we then take limits as $\Delta \to 0$ and $\tau \to 0$ jointly, with the ratio Δ^2/τ held constant [46]. In the continuum limit we obtain a pde which can be written as

$$\frac{\partial C}{\partial t} = D_0 \nabla \cdot [D(C) \nabla C] - \nabla \cdot [\mathbf{V}_0 V(C)], \qquad \text{(A3)}$$

where the diffusion coefficient and the nonlinear diffusivity are given by

$$D_0 = \left(\frac{P}{4}\right) \lim_{\Delta,\tau \to 0} \left(\frac{\Delta^2}{\tau}\right),$$

$$D(C) = (1-q)^{(4C)}[1 - 4C(C-1)\ln(1-q)]. \qquad \text{(A4)}$$

The components of the advective velocity, $\mathbf{V_0} = (v_x, v_y)$, and the nonlinear advective flux are given by

$$v_x = \left(\frac{P}{2}\right) \lim_{\Delta,\tau \to 0} \left(\frac{\rho_x \Delta}{\tau}\right), \quad v_y = \left(\frac{P}{2}\right) \lim_{\Delta,\tau \to 0} \left(\frac{\rho_y \Delta}{\tau}\right),$$

$$V(C) = (1-q)^{(4C)} C(1-C). \qquad \text{(A5)}$$

To obtain a well-defined continuum limit, we require that if ρ_x and ρ_y are nonzero and the motility is biased, these coefficients decrease to zero as $\rho_x = \mathcal{O}(\Delta)$ and $\rho_y = \mathcal{O}(\Delta)$ [14,46]. It is possible to derive the governing pde for this random-walk model on different lattices and for other spatial dimensions. Here, we focus on a 2D problem and a square lattice as this is sufficient to give us physical insight into the model.

This analysis gives us two different ways to view the discrete random-walk model. First, we can visualize stochastic simulations to demonstrate how individual agents interact with each other. This kind of visualization gives us insight into how the interactions between individual agents control the dynamics of the entire population. Results from several identically prepared simulations can be used to construct average agent density data to show how the average density evolves during the simulations [14,15]. Second, by solving Eq. (A3), we can directly predict the average behavior of the system.

We now present both stochastic simulations of the random-walk model together with solutions of Eq. (A3) to show how altering the adhesion parameter q affects the evolution of the system under unbiased and biased motility conditions. Equation (A3) is a nonlinear advection diffusion equation, and we solve this pde model numerically. The numerical solution of Eq. (A3) is obtained using a finite-difference method using a constant grid spacing δx and implicit Euler stepping with constant time steps δt. A central difference method is used to approximate the advection term. Picard iteration with convergence tolerance ε is used to solve the resulting nonlinear equations [14].

Unbiased motility. We first present results with $\rho_x = \rho_y = 0$, so that the motility of agents is unbiased. We consider simulations on a lattice with $1 \leq x \leq 400$ and $1 \leq y \leq 20$. Periodic boundary conditions are imposed at $y=1$ and $y=20$. Reflecting boundary conditions are imposed at $x=1$ and $x=400$. Initially, all sites where $180 \leq x \leq 220$ are occupied. Results in Figs. 3(a)–3(c) are for no adhesion, $q=0$; results in Figs. 3(d)–3(f) are for low adhesion, $q=0.25$; and results in Figs. 3(g)–3(i) are for a moderate amount of adhesion, $q=0.50$. In each case, snapshots of the agents at $t=0$ and $t=1000$ are given, and we can see that as q increases, the distance that the population of agents spreads in the x direction is reduced owing to agent-to-agent adhesion.

For each set of simulation results, we present agent density profiles in Figs. 3(c), 3(f), and 3(i). These density profiles are obtained from the simulation data by calculating the average occupancy of each column of the lattice, and then further averaging this column occupancy across $n=20$ identically prepared simulations [15,16]. These density profiles also show that the amount of agent spreading reduces as q increases. Numerical solutions of a one-dimensional (1D) form of Eq. (A3) with boundary and initial conditions matching the discrete simulations are given in Figs. 3(c), 3(f), and 3(i). We see that the column-averaged simulation data and the solution of the pde match very well.

Biased motility. We also present results with $\rho_x = 0.2$ and $\rho_y = 0$, so that the agents are more likely to move in the positive x direction rather than the negative x direction. This directed motion could represent some kind of tactic response. Simulations on the same lattice, with identical initial and boundary conditions for the unbiased motility mechanism, are considered. Results in Fig. 4 show the effects of different amounts of agent-to-agent adhesion. In each case, snapshots of the agents at $t=0$ and $t=1000$ are given, and we can see that the population of agents tends to drift in the positive x direction. We also see the effect of adhesion since the population of agents tends to move and spread less as q increases. For each set of simulation results, we present agent density profiles in Figs. 4(c), 4(f), and 4(i) that are column density data obtained from the simulations averaged across $n=20$ identically prepared realizations. This density information, derived from simulation data, shows that the amount of agent spreading reduces as q increases. Numerical solutions of a 1D form of Eq. (A3) with boundary conditions and initial conditions to match the discrete simulations are also given in

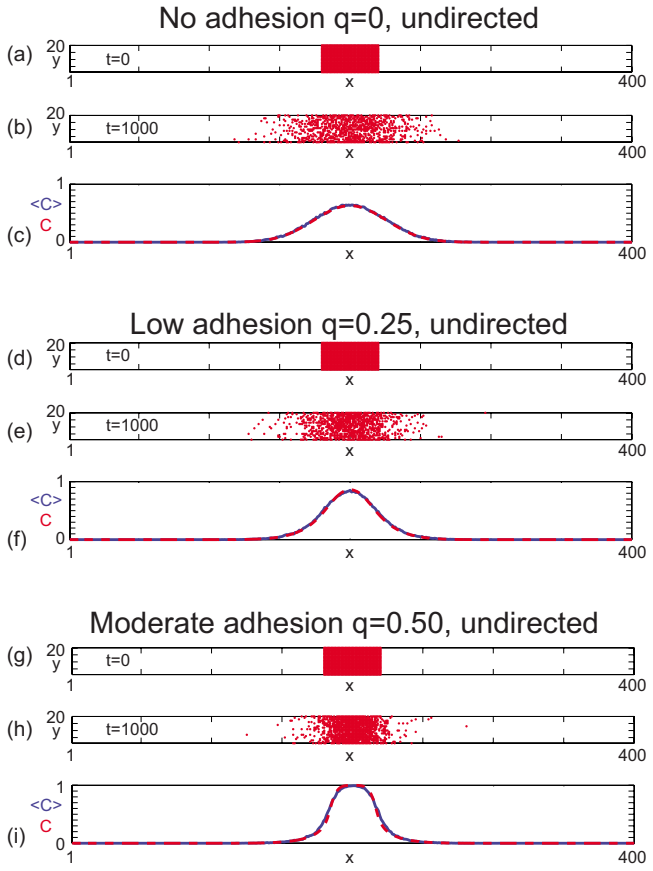

FIG. 3. (Color online) Simulation data demonstrate the effect of agent-to-agent adhesion in an undirected population of agents. All stochastic simulations correspond to $P=\Delta=\tau=1$. Results in (a) and (b) show the distribution of a population of agents with no agent-to-agent adhesion over a period of 1000 time steps. Column-averaged densities, further averaged over $n=20$ identically prepared realizations, are shown in the solid blue (solid gray) curve in (c) and compared with a numerical solution of Eq. (A3) shown in the dotted red (dotted gray) curve with the same initial conditions and boundary conditions used in the discrete simulations. In this work all numerical solutions are obtained with $\delta x=0.01=\delta t=0.01$ and $\epsilon=1\times10^{-6}$. Data in (d)–(f) and (g)–(i) show similar results for adhesive populations with $q=0.25$ and $q=0.50$, respectively.

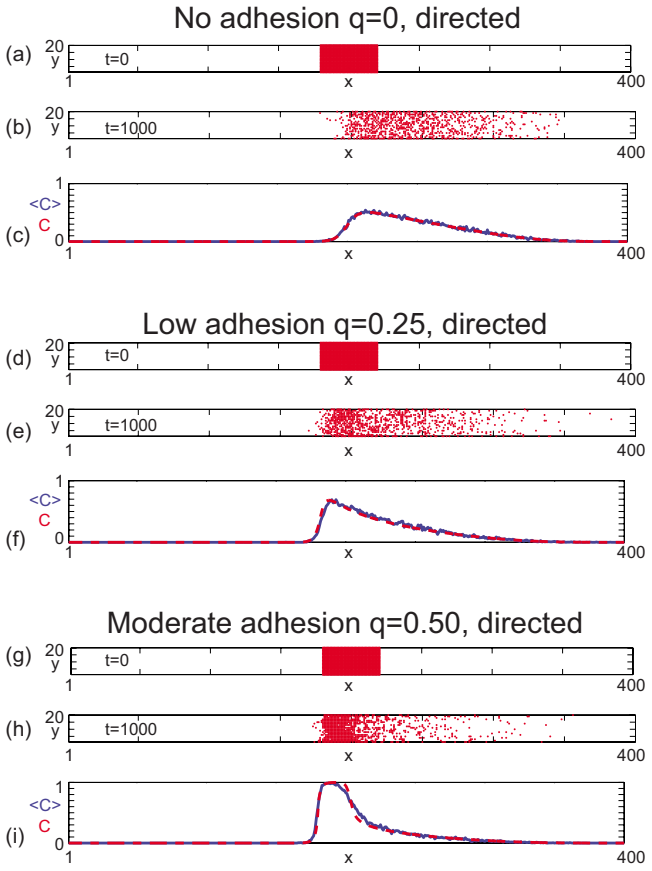

FIG. 4. (Color online) Simulation data demonstrate the effect of agent-to-agent adhesion in a directed population of agents. All stochastic simulations correspond to $P=\Delta=\tau=1$. Results in (a) and (b) show the distribution of a population of agents with no agent-to-agent adhesion over a period of 1000 time steps. Column-averaged densities, further averaged over $n=20$ identically prepared realizations, are shown in the solid blue (solid gray) curve in (c) and compared with a numerical solution of Eq. (A3) shown in the dotted red (dotted gray) curve with the same initial conditions and boundary conditions used in the discrete simulations. In this work all numerical solutions are obtained with $\delta x=0.01=\delta t=0.01$ and $\epsilon=1\times10^{-6}$. Data in (d)–(f) and (g)–(i) show similar results for adhesive populations with $q=0.25$ and $q=0.50$, respectively.

Figs. 4(c), 4(f), and 4(i) showing that the column-averaged simulation data and the solution of the pde match very well.

The key difference between the simulation data presented here and in the main text is that here we have no porous membrane. It is possible to derive a continuum pde model where the agent motility and bias parameters are spatially variable with $P=P(x,y,z)$, $\rho_x=\rho_x(x,y,z)$, $\rho_y=\rho_y(x,y,z)$, and $\rho_z=\rho_z(x,y,z)$. To do this we require that each function $P(x,y,z),\rho_x(x,y,z),\rho_y(x,y,z),\rho_z(x,y,z)$ is differentiable and can be expanded in a Taylor series. In the main text we represent the porous membrane by suppressing movements in the negative z direction along the plane where $k=1$. This means that the motility coefficients are not differentiable and we cannot derive a pde. Despite this difference, the physical insight gained by presenting simulation data, deriving the pde, and comparing the solution of the pde with averaged simulation data here gives us an appreciation of the discrete random-walk model.

All values of q considered in this work give $D(C)>0$ for $C\in[0,1]$. This is not always the case. For $q\in[0.64,1)$, Eq. (A4) shows that $D(C)<0$ for some values of $C\in[0,1]$. This transition to a nonlinear diffusivity that can be negative is associated with discontinuous solutions of Eq. (A3) [47] and the formation of agent clustering in the discrete simulations [15]. For the transwell assays we do not have to consider these complications because the value of q required to match the experimental data is sufficiently small ($q=0.1$) that the issue of negative diffusivities do not arise, and the continuum-discrete match is very good (Figs. 3 and 4). Further details about the relationship between this discrete mechanism and analytical conditions governing the formation of clusters have been described previously [11–13]. This previous work links the discrete mechanism to the Ising model and defines the region in the (q,C) parameter space for clustering. In comparison, our approximate continuum

model defines a different region in the (q,C) parameter space for clustering. Finally, we reiterate that the continuum-discrete comparison in Figs. 3 and 4 confirms that the continuum model developed here is valid when q is sufficiently small, $q \leq 0.5$. Further simulation data (not shown here) confirm that the continuum model fails to match the discrete data when q is sufficiently large, $q > 0.5$. The failure of our continuum model to predict the discrete simulations for large q is consistent with the fact that the continuum model predicts a different region in the (q,C) parameter space for clustering compared to the Ising model approach [11].

[1] M. Abercrombie, Nature (London) **281**, 259 (1979).
[2] A. Q. Cai, K. A. Landman, and B. D. Hughes, J. Theor. Biol. **245**, 576 (2007).
[3] M. Ward *et al.*, J. Neurosci. **23**, 5170 (2003).
[4] N. R. Druckenbrod and M. L. Epstein, Dev. Dyn. **236**, 84 (2007).
[5] P. K. Maini, D. L. S. McElwain, and D. I. Leavesley, Tissue Eng. **10**, 475 (2004).
[6] J. A. Sherratt and J. D. Murray, Proc. R. Soc. London, Ser. B **241**, 29 (1990).
[7] H. Sheardown and Y. L. Cheng, Chem. Eng. Sci. **51**, 4517 (1996).
[8] H. C. Berg, *Random Walks in Biology (Expanded Edition)* (Princeton University Press, Princeton, NJ, 1983).
[9] T. M. Liggett, *Stochastic Interacting Systems: Contact, Voter and Exclusion Processes* (Springer-Verlag, Berlin, 1999).
[10] T. Callaghan *et al.*, J. Stat. Phys. **122**, 909 (2006).
[11] E. Khain, L. M. Sander, and C. M. Schneider-Mizell, J. Stat. Phys. **128**, 209 (2007).
[12] E. Khain and L. M. Sander, Phys. Rev. E **77**, 051129 (2008).
[13] E. Khain *et al.*, EPL **88**, 28006 (2009).
[14] M. J. Simpson, K. A. Landman, and B. D. Hughes, Physica A **388**, 399 (2009).
[15] M. J. Simpson *et al.*, Physica A **389**, 1412 (2010).
[16] M. J. Simpson, K. A. Landman, and B. D. Hughes, Physica A **389**, 3779 (2010).
[17] K. J. Painter and T. Hillen, Can. Appl. Math. Q. **10**, 501 (2002).
[18] I. Tamm *et al.*, Proc. Natl. Acad. Sci. U.S.A. **91**, 3329 (1994).
[19] L. Wolpert, *Principles of Development*, 2nd ed. (Oxford University Press, Oxford, 2002).
[20] J. L. Kleinsmith, *Principles of Cancer Biology* (Pearson, San Francisco, 2006).
[21] N. J. Armstrong, K. J. Painter, and J. A. Sherratt, J. Theor. Biol. **243**, 98 (2006).
[22] F. Graner and J. A. Glazier, Phys. Rev. Lett. **69**, 2013 (1992).
[23] C. Deroulers, M. Aubert, M. Badoual, and B. Grammaticos, Phys. Rev. E **79**, 031917 (2009).
[24] H. D. Soule *et al.*, J. Natl. Cancer Inst. (1940-1978) **51**, 1409 (1973).
[25] Details at http://www.catalog2.corning.com/Lifesciences
[26] D. I. Leavesley *et al.*, J. Cell Biol. **117**, 1101 (1992).
[27] A. Noble *et al.*, Endocrinology **144**, 2417 (2003).
[28] H. Yu *et al.*, J. Clin. Lab Anal **13**, 166 (1999).
[29] S. Rajaram, D. J. Baylink, and S. Mohan, Endocr. Rev. **18**, 801 (1997).
[30] J. A. Kricker, Ph.D. thesis, Queensland University of Technology, 2004.
[31] Y. Gao *et al.*, J. Cancer Res. Clin. Oncol. **136**, 667 (2010).
[32] D. Meng *et al.*, Toxicol. Appl. Pharmacol. **244**, 291 (2010).
[33] L. M. Smith *et al.*, Oncogene **18**, 6063 (1999).
[34] R. L. Sutherland, R. E. Hall, and I. W. Taylor, Cancer Res. **43**, 3998 (1983).
[35] M. J. Simpson *et al.*, Dev. Biol. **302**, 553 (2007).
[36] J. D. Murray, *Mathematical Biology I: An Introduction*, 3rd ed. (Springer-Verlag, Heidelberg, 2002).
[37] H. M. Byrne, Nat. Rev. Cancer **10**, 221 (2010).
[38] D. Chowdhury, A. Schadschneider, and K. Nishinari, Phys. Life. Rev. **2**, 318 (2005).
[39] J. Zhang, S. Weiguo, and X. Xuan, Physica A **387**, 5901 (2008).
[40] K. R. Swanson *et al.*, Clin. Oncol. **20**, 301 (2008).
[41] M. J. Simpson, K. A. Landman, and T. P. Clement, Math. Comput. Simul. **70**, 44 (2005).
[42] I. R. Lapidus, J. Theor. Biol. **86**, 91 (1980).
[43] J. A. Sherratt, Bull. Math. Biol. **56**, 129 (1994).
[44] M. R. D'Orsogna, M. A. Suchard, and T. Chou, Phys. Rev. E **68**, 021925 (2003).
[45] M. J. Simpson *et al.*, J. Theor. Biol. **243**, 343 (2006).
[46] E. A. Codling, M. J. Plank, and S. Benhamou, J. R. Soc., Interface **5**, 813 (2008).
[47] T. P. Witelski, Appl. Math. Lett. **8**, 27 (1995).